AIAA JOURNAL
Vol. 30, No. 11, November 1992

Navier-Stokes Computation of Wing/Rotor Interaction for a Tilt Rotor in Hover

Ian Fejtek* and Leonard Roberts†
Stanford University, Stanford, California 94305

A method has been developed to analyze the wing/rotor interaction of tilt rotor aircraft in hover. The unsteady, thin-layer compressible Navier-Stokes equations are solved using an implicit, finite difference scheme that employs lower upper-alternating direction implicit factorization. The rotor is modeled as an actuator disk that imparts a radial and azimuthal distribution of pressure rise and swirl to the flowfield. The chimera approach of grid point blanking is used to update the rotor boundary conditions. Results are presented for both a rotor alone and for wing/rotor interaction where the thrust coefficient is 0.0164 and wing flap deflection is 67 deg. Many of the complex flow features are captured, including the transition from chordwise to spanwise flow on the wing upper surface, the fountain effect, the wing leading- and trailing-edge separation, and the large region of separated flow beneath the wing. Wing surface pressures compare fairly well with experimental data although the time-averaged download is somewhat higher than the measured value. Discrepancies with experimental results are due to a combination of factors that are discussed.

Introduction

TILT rotor aircraft such as the XV-15 and the V-22 are unique in that they combine the vertical takeoff and landing capability of the helicopter with the efficient high-speed cruise performance of fixed-wing turboprop aircraft. A major limitation of the design, however, is the download in hover that is produced by the rotor wake impinging on the fixed wing. This download, which is approximately 10% of the total rotor thrust, reduces payload carrying capability by as much as 40%.[1] It was the objective of this work to exploit current computational fluid dynamic techniques in order to obtain a better understanding of the complex tilt rotor flowfield in hover. Additionally, it was desired to develop a foundation from which such download reduction mechanisms as flap deflection and wing leading-edge tangential blowing could be studied.

The tilt rotor flowfield has been observed experimentally to possess many interesting features.[2] Because the rotor is only about one wing chord above the wing, the flowfields induced by the wing and the rotor are closely coupled. There exists a large region of nearly stagnated flow on the wing upper surface and a large region of unsteady, turbulent, separated flow beneath the wing. As can be seen in Fig. 1, taken from Ref. 3, the inboard-moving spanwise flow on the upper surface from both wing halves meets at the vehicle centerline and is redirected upward, creating a recirculation pattern referred to as the fountain effect. The rotor flow itself is very complicated. The rotor imparts not only a vertical downwash to the flowfield, but also, due to the rotational motion of the rotor, a velocity tangential to the circumferential direction called the swirl velocity. Regions of concentrated vorticity (tip vortices) which trail from the blade tips, propagate in a helical motion in the rotor wake, interacting with the following blades and also with the wing.

Accurate, simultaneous, numerical prediction of all of these flow features still lies beyond the state of the art. To render the problem tractable, simplifications were made. Only the wing and rotor were modeled. Since accurate modeling of the flow about the individual rotor blades is a complex task and a tremendous computational drain (see, e.g., Ref. 4), the rotor in this study was modeled as an actuator disk where the blade loads are averaged over elemental areas of the rotor disk. Because of the considerable extent of separated flow beneath the wing, viscous effects are significant and the Navier-Stokes equations are used to describe the flowfield. The form of these equations and the method of solution employed in this study are discussed briefly in the next sections.

Previous theoretical studies of airfoil and wing download in hover have either solved simpler fluid dynamic equations or restricted the analysis to two dimensions. Clark and McVeigh[5] and Clark[6] applied a low-order panel method to this problem. Many of the overall flow features were predicted. Because of the nature of the equations solved (Laplace's equation), however, their results must be viewed with some caution, as separated flows cannot be accurately predicted with this formulation without a priori knowledge of separation locations and total or dynamic pressures in the wake region. References 7 and 8 describe discrete-vortex seeding methods used to calculate the unsteady, two-dimensional flow around an airfoil at an angle of incidence of -90 deg by solving the vorticity transport equation. The upper surface pressures were computed fairly well but the lower surface base pressures did not compare favorably with experimental results. Raghavan et al.[9] performed two-dimensional Navier-Stokes computations on the XV-15 airfoil at -90 deg angle of incidence in a low Mach number and low Reynolds number freestream flow. The mean value of the computed cyclic download did not correspond well with experimental measurements. This was again due to difficulty in predicting the base pressure. It is anticipated that, in three dimensions, due to a less-constrained flowfield than in two dimensions, the vortex shedding and turbulence in the wing wake will be reduced in strength, and a more accurate prediction of the base pressures may be possible.

Governing Fluid Dynamic Equations

The partial differential equations used here to describe the tilt rotor flowfield are the thin-layer Navier-Stokes equations. Transformed into a generalized, body-fitted, curvilinear coordinate system (ξ, η, ζ, τ), and nondimensionalized with respect

---

Presented as Paper 91-0707 at the AIAA 29th Aerospace Sciences Meeting, Reno, NV, Jan. 7–10, 1991; received Jan. 22, 1991; revision received April 7, 1992; accepted for publication April 20, 1992.

*Graduate Research Assistant; currently Senior Engineer, De Havilland, Inc. Member AIAA.

†Professor, Department of Aeronautics and Astronautics. Member AIAA.

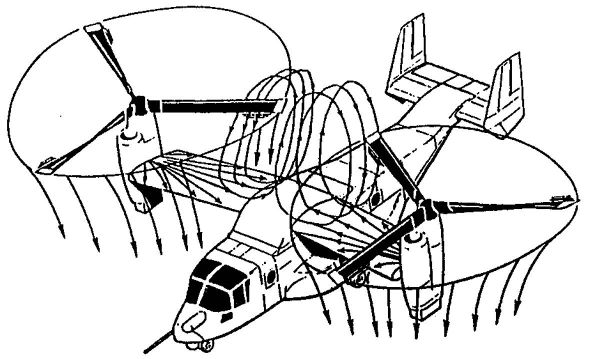

Fig. 1 Sketch of the V-22 in hover, showing the main flow features (taken from Ref. 3).

to freestream ambient flow values, these equations can be written in conservation-law form[10] as

$$\frac{\partial \hat{Q}}{\partial \tau}+\frac{\partial \hat{E}}{\partial \xi}+\frac{\partial \hat{F}}{\partial \eta}+\frac{\partial \hat{G}}{\partial \zeta}=\frac{1}{Re}\frac{\partial \hat{G}_v}{\partial \zeta} \tag{1}$$

where $\hat{Q}$, the vector of conserved quantities, is $\hat{Q} = J^{-1}\,[\rho \;\rho u\; \rho v\; \rho w\; e]^T$ and

$$\hat{E}=\frac{1}{J}\begin{bmatrix}\rho U\\ \rho u U+\xi_x p\\ \rho v U+\xi_y p\\ \rho w U+\xi_z p\\ (e+p)U-\xi_t p\end{bmatrix}, \qquad \hat{F}=\frac{1}{J}\begin{bmatrix}\rho V\\ \rho u V+\eta_x p\\ \rho v V+\eta_y p\\ \rho w V+\eta_z p\\ (e+p)V-\eta_t p\end{bmatrix}$$

$$\hat{G}=\frac{1}{J}\begin{bmatrix}\rho W\\ \rho u W+\zeta_x p\\ \rho v W+\zeta_y p\\ \rho w W+\zeta_z p\\ (e+p)W-\zeta_t p\end{bmatrix}, \qquad \hat{G}_v=\frac{1}{J}\begin{bmatrix}0\\ \zeta_x\tau_{xx}+\zeta_y\tau_{xy}+\zeta_z\tau_{xz}\\ \zeta_x\tau_{yx}+\zeta_y\tau_{yy}+\zeta_z\tau_{yz}\\ \zeta_x\tau_{zx}+\zeta_y\tau_{zy}+\zeta_z\tau_{zz}\\ \zeta_x\beta_x+\zeta_y\beta_y+\zeta_z\beta_z\end{bmatrix}$$

The Cartesian velocity components u, v, w are nondimensionalized with respect to the freestream speed of sound a_∞, density ρ is normalized by ρ_∞, and the pressure p and total energy e by $\rho_\infty a_\infty^2$. The contravariant velocity components U, V, W, the Jacobian J, and the metrics ξ_x, η_y, ζ_z, etc., all result from the coordinate transformation. The quantities τ_{xx}, τ_{xy}, etc., are the components of the shear stress, and β_x, β_y, β_z are functions of the shear stress and internal energy. The Reynolds number Re is based on the freestream sound speed a_∞ and the wing chord c. The system of equations is closed by relating the pressure to the conservative flow variables through the equation of state for a perfect gas:

$$p=(\gamma-1)[e-\rho/2(u^2+v^2+w^2)] \tag{2}$$

where γ is the ratio of specific heats. The dynamic viscosity μ is composed of two parts—a laminar viscosity contribution estimated by Sutherland's law, and a turbulent viscosity evaluated here using the Baldwin-Lomax algebraic eddy-viscosity model.

Numerical Algorithm

The numerical algorithm used in this work to solve the three-dimensional compressible thin-layer Navier-Stokes equations discussed earlier is an implicit, time-accurate scheme referred to as lower upper-alternating direction implicit (LU-ADI) factorization and developed by Fujii and Obayashi.[11,12] The algorithm has been extended in this work in a manner similar to the solution blanking of the chimera technique adopted in Ref. 13. This allows desired regions of the computational domain to be excluded from the implicit solution. Values of the solution vector at these blanked locations are then updated explicitly using values obtained from an independent analysis. This is a very convenient and effective means of modeling the rotor, as is discussed in greater detail later. The numerical algorithm is briefly outlined in the following.

The Beam-Warming method of approximate factorization is applied to Eq. (1):

$$\begin{aligned}&[I+i_b h\delta_\xi A^n-i_b D_i|_\xi][I+i_b h\delta_\eta B^n-i_b D_i|_\eta]\\ &\quad\times[I+i_b h\delta_\zeta C^n-i_b h Re^{-1}\delta_\zeta J^{-1}M^n J-i_b D_i|_\zeta]\Delta\hat{Q}^n\\ &\quad=-i_b h[\delta_\xi E^n+\delta_\eta F^n+\delta_\zeta G^n-Re^{-1}\delta_\zeta G_v^n]\\ &\quad-i_b[D_e|_\xi+D_e|_\eta+D_e|_\zeta]\hat{Q}^n\end{aligned} \tag{3}$$

where I is the identity matrix, h the time step, and n the previous time level. D_i and D_e are, respectively, the implicit and explicit artificial dissipation terms required for numerical stability. Also, δ is a second-order central difference operator. The algorithm is first-order accurate in time and second-order accurate in space. The flux Jacobian matrices A, B, C, and M arise from the local linearization of the flux vectors about the solution vector at the previous time level. The equations are solved in delta form where $\Delta\hat{Q}^n = \Delta\hat{Q}^{n+1} - \hat{Q}^n$. The integer i_b is assigned a value of zero or one at every grid point. If $i_b = 0$, then $\Delta\hat{Q}^n$ at this grid location becomes zero and the solution at this point is updated explicitly; if $i_b = 1$, the location is not blanked and the implicit treatment of the solution remains unchanged.

Each ADI operator forms a block tridiagonal matrix. Applying a matrix diagonalization introduced by Pulliam and Chaussee,[14] the matrix in each of the three directions can be reduced to a scalar tridiagonal, thereby considerably enhancing computational efficiency. For example, in the ξ direction, the operator becomes

$$[I+i_b h\delta_\xi A^n-i_b D_i|_\xi]=T_\xi[I+i_b h\delta_\xi\Lambda_A-i_b J^{-1}\epsilon_i\delta_\xi^2 J]T_\xi^{-1} \tag{4}$$

where second-order implicit smoothing has been prescribed. Because of the hyperbolic nature of the flux Jacobian matrices, A, for example, can be diagonalized by a similarity transformation, i.e., $\Lambda_A = T_\xi A T_\xi^{-1}$, where T_ξ is the transformation matrix and Λ_A is a diagonal matrix containing the eigenvalues of A. The implicit smoothing factor ϵ_i is a product of a user-specified constant, the time step, and the spectral radius of Λ_A.

The central differencing is decomposed into two one-sided differences using the flux vector splitting technique of Steger and Warming.[15] The ξ-direction operator becomes

$$=T_\xi[I+i_b\Delta_\xi\Lambda_A^+ +i_b\nabla_\xi\Lambda_A^-]T_\xi^{-1} \tag{5}$$

where

$$\Lambda_A^\pm=h/2(\Lambda_A\pm|\Lambda_A|)\pm\underline{J}^{-1}\epsilon_i J$$

and ∇_ξ and Δ_ξ are backward and forward differences, respectively. The inverse of the Jacobian, $\underline{J}^{-1}$, is evaluated at the center point j.

Employing first-order-accurate differencing, and rearranging:

$$=T_\xi\Bigg[\underbrace{-i_b\Lambda_{A_{j-1}}^+}_{L_A}+\underbrace{I+i_b(\Lambda_{A_j}^+-\Lambda_{A_j}^-)}_{D_A}+\underbrace{i_b\Lambda_{A_{j+1}}^-}_{U_A}\Bigg]T_\xi^{-1} \tag{6}$$

By applying diagonally dominant factorization,[16]

$$L_A+D_A+U_A=(L_A+D_A)D_A^{-1}(D_A+U_A)+O(h^2) \tag{7}$$

The second-order error is consistent with the previous approximations.

Finally, the ξ-direction ADI operator becomes

$$T_\xi \underbrace{[L_A + D_A]}_{\text{lower bidiagonal}} \underbrace{[D_A^{-1}(D_A + U_A)]}_{\text{upper bidiagonal}} T_\xi^{-1}$$

$$= T_\xi [I + i_b(\nabla_\xi \Lambda_A^+ - \Lambda_{A_j}^-)][I + i_b h \, | \Lambda_A |]^{-1}$$

$$\times [I + i_b(\Delta_\xi \Lambda_A^- + \Lambda_{A_j}^+)] T_\xi^{-1} \tag{8}$$

A similar procedure is followed for the η and ζ directions. The matrix inversion for each direction has been reduced to a product of a lower and an upper scalar bidiagonal matrix. It is implemented by performing a forward sweep followed by a backward sweep. The procedure is modified in the ζ direction because the flux Jacobian matrices C and M are not simultaneously diagonalizable.[10] The implicit viscous terms in the ζ-direction ADI operator are neglected, and the split diagonal matrices $\Lambda_C^\pm$ are modified slightly to ensure numerical stability.[12] Neglecting the matrix M does not affect the converged steady-state solution ($\Delta \hat{Q}^n \to 0$) because the right-hand side of Eq. (3) remains unchanged. Obayashi and Guruswamy[17] used the LU-ADI solution algorithm similar to that described here to validate the method for viscous flows, which are also unsteady.

The numerical computation of the flux derivatives and transformation metrics using central differences for three-dimensional problems introduces small errors due to violation of flow conservation. Typically, freestream values of the fluxes are subtracted from the governing equations to achieve perfect freestream capture.[10] In the present hover computation, however, where the flow at the far-field boundary is nonuniform and near zero, an approach suggested by Vinokur[18] and implemented for plume flows with nonuniform freestream by Obayashi[19] is more appropriate. By computing the metrics and Jacobian at each point by using a finite volume approach over a distance of two grid cell widths in each direction, and by evaluating the flux derivatives using second-order-accurate central differencing, freestream preservation is ensured.

An artificial dissipation model[20] based on a nonlinear combination of fourth-order and second-order smoothing to reduce oscillations near flow discontinuities without introducing excessive diffusion is used for the right-hand side of Eq. (3).

Grid Generation

The three-dimensional grid used for the computations discussed here was generated by stacking vertical, parallel, two-dimensional grids at spanwise locations along the wing and beyond the wingtip. A Poisson equation solver[21] was used to create the smoothed two-dimensional grids and to cluster the points near the airfoil and the rotor. O-grids were selected as they offered the most desirable grid point distribution for this type of flowfield where large flow gradients occur around both the leading and the trailing edge.

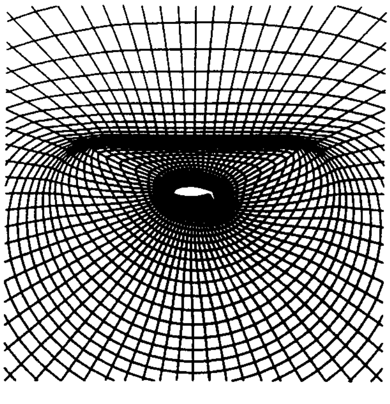

Fig. 2 Cross-sectional cut through mesh showing the concentration of grid points around wing and rotor.

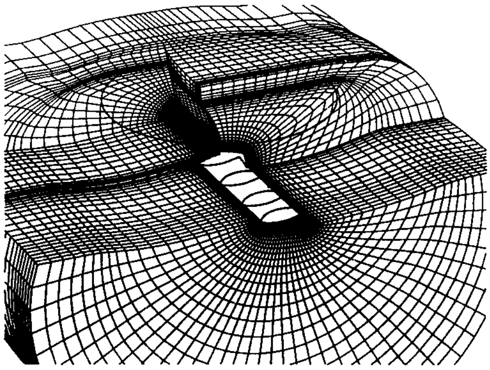

Fig. 3 Cutaway view of mesh showing wing and rotor locations.

Figure 2 is a view of one of the typical two-dimensional grids used to make up the complete three-dimensional grid. Although only one zone, the smoothing was actually carried out independently on two separate meshes to obtain the desired grid spacing in the location of the rotor: 1) an inner grid whose inner boundary was the airfoil surface and whose outer boundary was the circumferential grid line containing the flattened upper portion used to define the rotor location, and 2) an outer grid enveloping the first grid and extending to a circular outer boundary 15 wing chords from the airfoil.

The V-22 wing is of constant cross section with a squared wingtip. To minimize discontinuities in the three-dimensional grid, the wing cross section was gradually reduced to a point on the outer 3% of the wing semispan, using five parallel two-dimensional grid planes. The grid, outboard of the wingtip, collapses to a singular line. This and other features of the grid can be better appreciated in Fig. 3, a perspective cutaway view of portions of the three-dimensional grid. The vertical grid plane in the foreground is the plane of symmetry. The outer edge of the rotor disk is superimposed on the grid to help visualize the position of the rotor with respect to the wing. The grid size is 73 × 47 × 70. There are 73 points that define the airfoil cross section in the ξ direction. Forty-seven two-dimensional grid planes are stacked in the spanwise η direction, 23 of which are on the wing. The ζ index extends normal from the wing surface through the plane of the rotor, where it has a value of 46, to the outer boundary, where it reaches a value of 70.

Boundary Conditions

In the current implementation of the solution algorithm, all boundary conditions are applied explicitly. Because of the symmetry of the flowfield in hover about the configuration centerline, only one-half of the tilt rotor was modeled. A plane of symmetry was specified by simply mirroring the interior flow solution about the wing root grid plane. No-slip boundary conditions were specified for the wing surface. Pressure at the surface was extrapolated from values in the flow interior by assuming zero normal pressure gradient. Also, because of the adiabatic conditions, density at the wall was obtained using zero-order extrapolation. The total energy was then calculated from Eq. (2). Beyond the wingtip, the values of $\hat{Q}$ on the singular line were determined by averaging the flow properties computed at the grid locations adjacent to and surrounding the singular line. The periodic boundary of the O-grid was updated at each spanwise grid location by averaging the flowfield solution at the grid points on both sides of the periodic boundary.

Typically for nonzero freestream flows, the outer boundary of the computational domain is divided into inflow and outflow regions as determined by a characteristics-type approach for evaluating consistent boundary conditions. In this hover

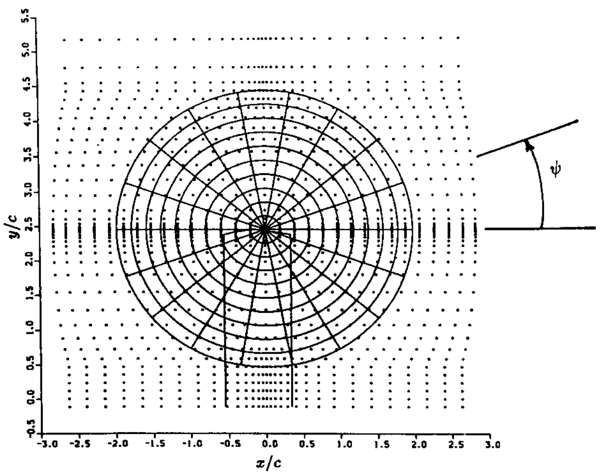

Fig. 4 Top view of grid points in rotor plane superimposed with the outline of the subdivided actuator disk.

case, however, where the flowfield is being driven solely by the rotor situated near the center of the computational domain, the entire outer boundary was treated as an outflow boundary. The only constraint imposed on the outer flowfield, then, was the static pressure, which was set to its freestream ambient value. All other flow properties at the outer boundary were obtained by zero-order extrapolation.

Rotor Model

The rotor is assumed to be an actuator disk—the blade loads are time and space averaged over elemental areas that comprise the entire rotor disk. Classic momentum theory/blade element analyses applied to actuator disk models of propellers and rotors (see, e.g., Glauert[22] or Prouty[23]) assume that there is no slip-stream contraction and that the flow through the rotor disk has no radial component. They generally allow only radial variations of torque and thrust. The momentum theory/blade element analysis presented here, on the other hand, allows the computation of slip-stream contraction. A radial component of flow is permitted, although, for the purpose of evaluating the aerodynamic forces on the rotor blades, only the axial and tangential flow components are taken into account. Also, the method discussed in the following computes both azimuthal and radial variations of torque and thrust.

Figure 4 is a view of those points of the computational grid that lie in the plane of the rotor. Superimposed on the figure is an outline of the wing and also the rotor disk, which has been subdivided uniformly into 10 radial and 18 azimuthal segments. At each time step of the solution procedure, at each elemental area on the rotor disk, an average of each of the flow properties is determined from the most recently computed Navier-Stokes solution at all points within the elemental area. Momentum theory/blade element analysis is then applied, which yields updated flow properties that are then specified at all points within the given area, for the next pass through the Navier-Stokes solver. This approach allows the incorporation of the effects of blade geometry, airfoil aerodynamic characteristics, blade twist and pitch (collective) angles, and rotor rotational speed, as described in the following. In this way, the influence of the rotor can be described by distributions of local pressure rise through the rotor and local swirl velocity. This approach has similarities with the method described in Ref. 24, where two-dimensional blade section characteristics are employed in the rotor model. In Ref. 24, however, source terms are added to the incompressible Navier-Stokes equations to compute the three-dimensional, time-averaged, rotor flow in forward flight.

Relative flow angles and resultant aerodynamic forces acting on an elemental area of the rotor disk are shown in Fig. 5. The analysis has been generalized here to include ascending and descending flight. The swirl velocity above the rotor disk is zero, and immediately downstream it jumps to V_t. Therefore, in the rotor plane, the swirl is assumed to be $V_t/2$. Each elemental area $\mathrm{d}A$ sweeps through an angle $\mathrm{d}\psi$ and possesses a radial width $\mathrm{d}r$ (i.e., $\mathrm{d}A = r\,\mathrm{d}\psi\,\mathrm{d}r$). The elemental thrust $\mathrm{d}T$ acting on $\mathrm{d}A$ is equal to the total load generated by all three blades on an annulus of the rotor disk (situated a distance r from the axis of rotation), multiplied by the factor $\mathrm{d}\psi/2\pi$, which represents the average time spent over each elemental area. This yields

$$\mathrm{d}T = B\,\frac{\mathrm{d}\psi}{2\pi}\,[L\cos(\phi+\alpha_i) - D\sin(\phi+\alpha_i)] \tag{9}$$

where B is the number of blades, and L and D are, respectively, the aerodynamic lift and drag forces produced by a rotor blade segment of width $\mathrm{d}r$. Referring to Fig. 5, the angle ϕ is zero in hover, and the angle α_i is the induced angle of incidence. In terms of the aerodynamic force coefficients, $L = \frac{1}{2}\rho V_{\text{eff}}^2 C_l c\,\mathrm{d}r$ and $D = \frac{1}{2}\rho V_{\text{eff}}^2 C_d c\,\mathrm{d}r$, where V_{eff} is the effective local velocity and c is the local blade chord. Both α_i and V_{eff} are in the plane normal to the radius and are determined from the most current Navier-Stokes solution. C_l and C_d are two-dimensional aerodynamic coefficients of lift and drag, respectively. In the current implementation, they are determined from a look-up table comprised of actual wind-tunnel test results for the airfoil sections that define the V-22 rotor blade. C_l and C_d are functions of the local angle of incidence α and the local Mach number. The pressure rise through the rotor at each elemental area is then given by $\Delta p = \mathrm{d}T/\mathrm{d}A$.

Note that from Fig. 5, $\alpha = \beta + \theta - (\phi + \alpha_i)$, where θ is the local blade twist relative to that at the 75% span location, and β is the blade pitch angle setting. A simple iterative root finding scheme is employed at each time step of the Navier-Stokes solution to determine β for a desired thrust coefficient C_T.

The local tangential (or swirl) velocity V_t is determined in a similar fashion. The elemental torque $\mathrm{d}Q$, referring to Fig. 5, is

$$\mathrm{d}Q = B\,\frac{\mathrm{d}\psi}{2\pi}\,[L\sin(\phi+\alpha_i) + D\cos(\phi+\alpha_i)]r \tag{10}$$

Another expression for $\mathrm{d}Q$ can be derived by considering the conservation of angular momentum. The torque produced by an elemental area of the rotor disk on the fluid is equal to the rate of change of angular momentum (the mass flow multiplied by the net circumferential change in velocity multiplied by the moment arm r):

$$\mathrm{d}Q = \underbrace{\rho(r\,\mathrm{d}\psi\,\mathrm{d}r)(V_a + V_\infty)}_{\text{mass flow}}\ \underbrace{V_t}_{\text{velocity change}}\ r \tag{11}$$

where V_a is the component of the local induced velocity normal to the rotor disk and, for hover, $V_\infty = 0$. Given $\mathrm{d}Q$ computed from Eq. (10), V_t can be obtained from Eq. (11).

Now that the pressure rise Δp and swirl velocity V_t have been computed, they are applied as interior boundary conditions, as described later. It is noted that, to avoid problems

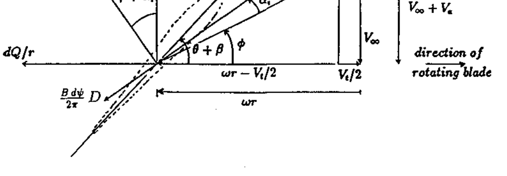

Fig. 5 Relative velocities and forces at an elemental area of the rotor disk.

associated with starting transients, the solution procedure is initiated by assuming that the rotor is uniformly loaded and the swirl is zero, i.e., $\Delta p = T/A$ and $V_t = 0$ for all elemental areas of the actuator disk. When the computed rotor downwash is well developed, the nonuniform rotor loading model is applied, and Δp and V_t are determined as described earlier.

Because rotor thrust is a function not of absolute static pressures, but of the change in pressure through the rotor disk, two adjacent horizontal layers of grid points are used to specify the desired flow conditions. As previously mentioned, a chimera-like approach is taken where the two layers of rotor grid points, i.e., those points closest to the plane of the rotor and that lie within the rotor radius, are blanked out of the implicit solution process (i.e., i_b is set to zero), and their flow values updated explicitly. The lower and upper layers of rotor grid points (separated by a vertical distance of 1% wing chord) are referred to in the following discussion as L and $L + 1$, respectively.

An approach similar to that used in Ref. 25 is adopted here to define a consistent set of boundary conditions for the rotor. Consideration of the characteristic velocities of the flowfield indicates that, for a subsonic inflow boundary, four flow properties must be specified and one can be extrapolated from the interior solution domain. The rotor grid points of layer L are considered to be an inflow boundary. The x component of velocity is a combination of the u velocity at $L + 1$ plus the component of swirl in the x direction. Similarly, the y component of velocity is a combination of the v velocity at $L + 1$ plus the component of swirl in the y direction. They are given in the following, assuming a counterclockwise rotation of the rotor as seen from above (as for the V-22):

$$u|_L = u|_{L+1} - V_t \sin\psi$$
$$v|_L = v|_{L+1} + V_t \cos\psi \tag{12}$$

The angle ψ is the angular location of a given rotor grid point with respect to a horizontal line extending aft from the rotor axis of rotation (see Fig. 4). The pressure is defined to be $p|_L = p|_{L+1} + \Delta p$. Because of the relatively light loading of the rotor in hover, the induced flow is of a low subsonic Mach number—i.e., the flow is near incompressible. In the absence of experimental data giving the total pressure or total temperature rise through the rotor, the density ρ is assumed, with negligible error, to be freestream ambient. The mass flow normal to the rotor disk $\rho w|_L$ is updated by applying zero-order extrapolation using the solution at $L - 1$.

The row $L + 1$ of rotor grid points is considered to be an outflow boundary where four flow properties are extrapolated and one is fixed. The density ρ, the mass fluxes ρu and ρv, and the total energy e are updated using zero-order extrapolation from the solution at $L + 2$. Mass continuity through the rotor disk is ensured by setting $\rho w|_{L+1} = \rho w|_L$.

Discussion of Results

Rotor Alone

Before considering wing/rotor interaction, the ability of the method to predict the flowfield of a rotor alone was examined. A Cartesian grid was created whose outer boundaries extend five rotor radii from the rotor axis of rotation in the horizontal and vertical directions. The grid has dimensions of 47 × 47 × 47 with most of the grid points clustered in the region of the rotor disk. On each of the two principal axes on the rotor disk are defined 26 points along the rotor diameter. The grid spacing is stretched vertically from a minimum of $0.01R$ at the plane of the rotor to $0.4R$ at the top and bottom boundaries (R is the rotor radius). Although a cylindrical grid would be more appropriate for the axisymmetric rotor alone flowfield, a Cartesian grid is used here because it is more representative of the grid point distribution used to resolve the rotor flow in the wing/rotor computations discussed later.

Figures 6–8 show various features of the computed flowfield for the V-22 rotor operating at a thrust coefficient of 0.0164 with a tip Mach number of 0.72 (these values are typical for a tilt rotor in hover). Figure 6 shows the projection of the velocity vectors onto a vertical plane through the rotor centerline. The cross section of the rotor disk, whose dimensions have been normalized with respect to rotor radius, has been superimposed on the plot. Note the changing flow angles as the rotor disk is approached from above. Grid points were concentrated near the rotor tip to help resolve the edge of the rotor wake. Beneath the rotor, however, the flow velocity drops rather gradually to the quiescent conditions outside the rotor wake. This diffusion of the flowfield is due to a combination of numerical and artificial dissipation. A finer mesh would be required to better resolve the shear layer formed between the inner and outer flowfields.

Figure 7 shows the Mach contours in a vertical plane through the rotor centerline. Note the flow acceleration from a quiescent state above the rotor to a maximum velocity below the rotor. The maximum induced velocity closely approximates that calculated using simple momentum theory assuming an effective uniform pressure rise. The flowfield is driven solely by the pressure rise at the rotor disk. Far above the

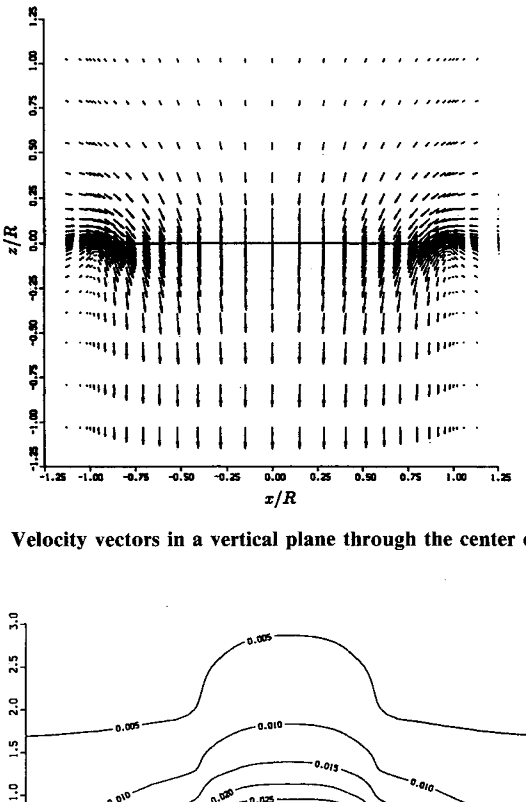

Fig. 6 Velocity vectors in a vertical plane through the center of the rotor.

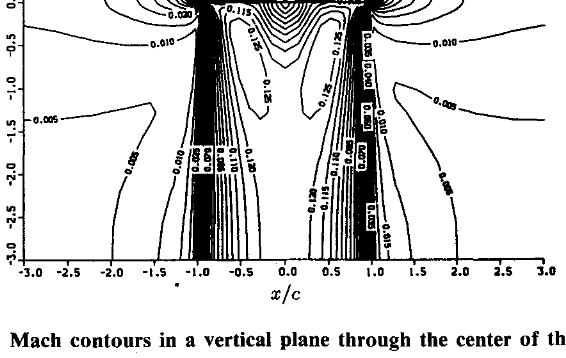

Fig. 7 Mach contours in a vertical plane through the center of the rotor.

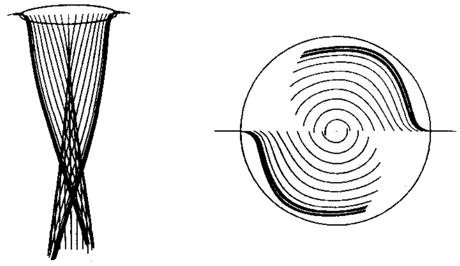

Fig. 8 Two views of particle traces in rotor wake showing the effect of swirl.

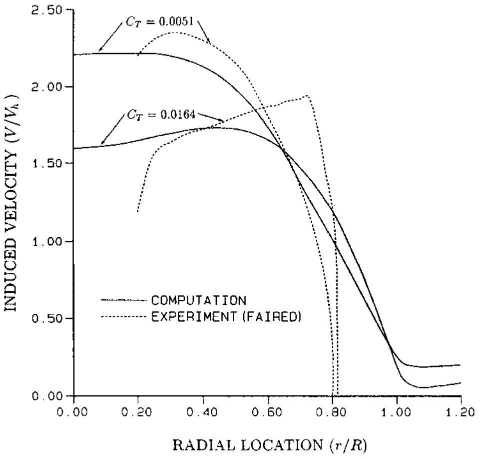

Fig. 9 Comparison of calculated and measured induced velocities about one wing chord below the rotor disk.

rotor, the pressure is freestream ambient, and below the rotor as the wake reaches its maximum speed, freestream ambient pressure is again approached. The presence and influence of the nacelle and rotor hub have been neglected in these computations. The current rotor model assumes that, in the region of the hub, the blade chord c and twist θ are linear extrapolations of their actual values at the edge of the hub at $r/R \approx 0.09$, inboard to the rotor centerline at $r/R = 0$.

Particles were seeded into the flowfield at every grid point on the rotor centerline immediately above the rotor. Figure 8 shows two views of the particle traces clearly demonstrating the effect on the flowfield of the swirl imparted at the rotor disk. The wake contraction is clearly evidenced. The traces terminate as the flow exits the lower computational boundary.

The comparisons discussed in the following are made with experimental results obtained from a test of an isolated 0.658-scale V-22 rotor in hover mode, at the Outdoor Aerodynamic Research Facility (OARF) of NASA Ames Research Center, and reported in Refs. 2 and 26. Figure 9 is a plot of the induced velocity as a function of radial location. The induced velocities are those in a horizontal plane below the rotor at a vertical location that corresponds to the position of the wing of the V-22 tilt rotor configuration. The velocities are normalized by V_h, the ideal induced velocity at the rotor disk in hover, where $V_h = \omega R\sqrt{C_T/2}$ and ωR is the rotor tip speed. The results for two different thrust coefficients are presented. Experimental tests[2] have shown that the radial distribution of induced velocity is sensitive to the thrust coefficient. For the twist distribution of the V-22 rotor blades, as C_T and the corresponding blade pitch angle increase, the local aerodynamic blade loading becomes greater in the outboard region of the rotor, thereby inducing greater velocities in the outer portion of the rotor slip stream. At low thrust coefficients, the inboard region is more highly loaded. As can be seen from Fig. 9, these trends with C_T are predicted numerically, although the absolute velocities differ somewhat from the experimental measurements. The computed velocities extend to the rotor centerline because, as previously mentioned, the nacelle has not been modeled. The Cartesian mesh, used to resolve the cylindrical rotor flow, contributes to the numerical diffusion of the slip-stream shear layer, preventing a more accurate prediction of induced velocities.

Figure 10 shows a comparison of rotor figure of merit between computational and experimental results. Figure of merit is a measure of hovering efficiency defined as the ratio of the minimum possible power required to hover (induced power) to the actual power required to hover (induced plus profile power). The experimental values of figure of merit are predicted reasonably well by the numerical computation over a range of rotor thrust coefficients.

The preceding results show that, despite the simplifications inherent in the rotor model and the less than optimum grid resolution, the current actuator disk model of the rotor simulates the expected overall flowfield behavior fairly well.

Wing/Rotor Interaction

The results discussed in this section are from computations of wing/rotor interaction in hover. The geometry of the V-22 wing/rotor configuration is used as a basis for the numerical model. There are, however, notable differences. To simplify the grid generation, the fuselage, tail, nacelle, and rotor hub are not modeled. The 6 degrees of forward sweep of the V-22 wing is also not modeled. The wing and rotor are assumed to be coplanar when they are actually angled 6 degrees with respect to each other. The nacelle is not modeled, and the rotor axis of rotation is placed at the wing tip (55%c aft of the leading edge)—not displaced outboard a distance equal to the nacelle half-width as in the actual configuration. This is in anticipation of future comparison of results with those obtained from NASA Ames tests of a simplified 0.16-scale wing/rotor configuration (which has no nacelle). The rotor radius of the numerical model is therefore reduced by the nacelle half-width to keep the extent of the rotor disk which lies above the wing essentially the same for both the actual and the computational configurations. Normalized by the wing chord, the effective rotor radius is 1.98, the effective wing semispan is 2.45, and the rotor height above the wing is 1.10 (an average of the varying height of the V-22 rotor disk above the wing). The wing is of constant chord with an airfoil section having a thickness/chord ratio of 0.23. To allow comparison with available experimental results, a flap deflection of 67 deg was selected. The grid, described previously, has over 240,000 points.

The results discussed here are for a case where the rotor thrust coefficient is 0.0164 and the rotor tip Mach number is 0.72. The Reynolds number based on wing chord c and the ideal induced velocity in the rotor plane V_h is 2.6×10^6.

Figure 11 is a perspective view of the computed velocity vectors on the near-vertical computational grid plane that runs

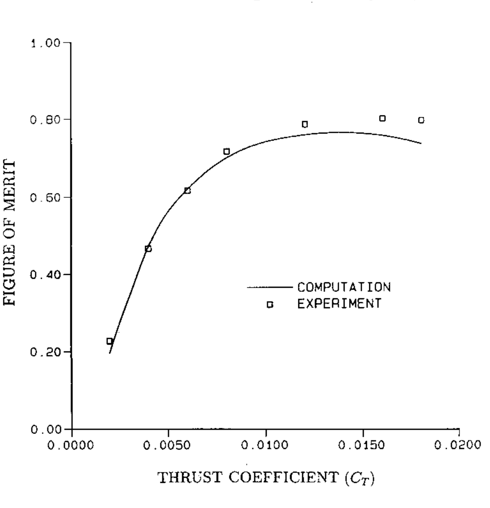

Fig. 10 Comparison of calculated and measured values of figure of merit for a range of thrust coefficients for the isolated rotor.

through the wing midchord line. The viewpoint is outboard of the wingtip and ahead of and above the wing. Flow acceleration through the rotor disk is clearly evidenced as is the flow stagnation on the wing upper surface. Close examination of the region below the wingtip shows the existence of a standing vortex. A recirculating-flow pattern is also visible above the wing adjacent to the plane of symmetry. This fountain flow is more clearly seen in Fig. 12, which shows the instantaneous particle traces in a vertical plane in the wing root region. Limited experimental flow visualization obtained in a 0.658-scale V-22 wing and rotor test at the NASA Ames OARF[26] indicates that the recirculation pattern has a larger radius. The vertical component of velocity was observed to be positive (upward) as far as two chords above the wing, as compared to about one chord in the present computation. The difference can at least partially be explained by the presence of the large wing/fuselage fairing in the experimental model, which tends to increase the portion of the flow that is redirected upward.

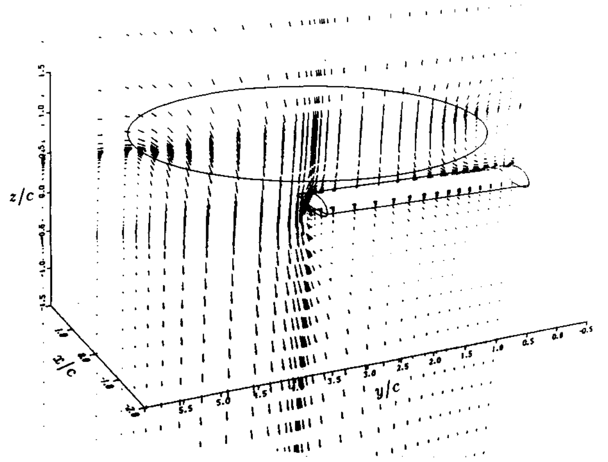

Fig. 11 Perspective view of the velocity vectors for wing/rotor interaction in a vertical plane running spanwise through the wing midchord.

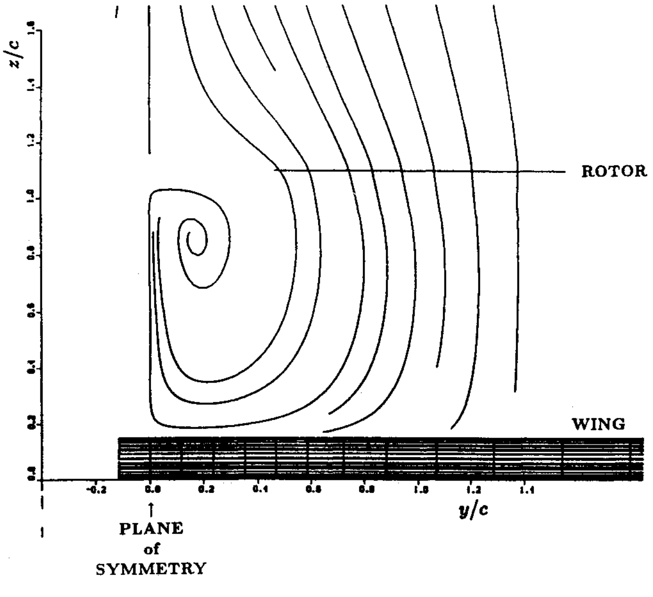

Fig. 12 View of instantaneous particle traces in a vertical plane through the wing midchord showing the computed fountain effect.

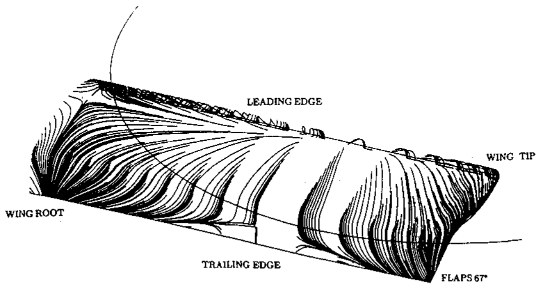

Fig. 13 Perspective view of oil flow on wing upper surface showing partial-span separation on the deflected flap.

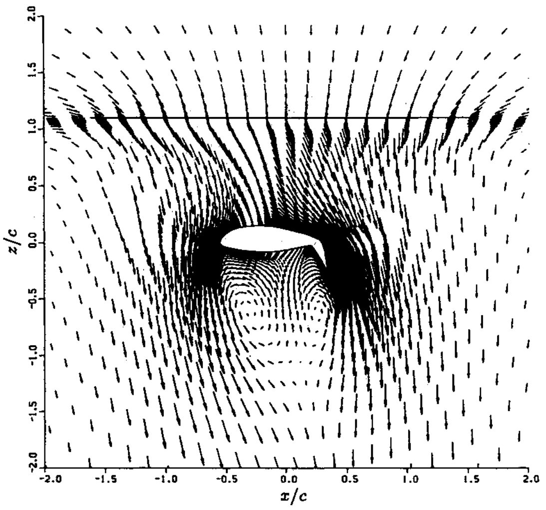

Fig. 14 Instantaneous velocity vectors at $2y/b = 0.53$.

Figure 13 is a perspective view of the computed oil flow pattern on the wing upper surface, as seen looking toward the flap from beyond the wingtip. The flow is primarily chordwise in the outer region of the wing and becomes more spanwise inboard. At the wing centerline, the flow is redirected fore and aft as indicated by the oil traces and also vertically upward to form the fountain flow. Flow visualization from the OARF test[26] indicates that the two-dimensional behavior extends to the wingtip, whereas the computation yields considerable spanwise flow over the tip. This discrepancy may be due, at least in part, to the flow straightening effects of the nacelle and large, flat model support structure used in the test. In the three-quarter semispan region, where the flow is primarily chordwise, the flow separates on the flap due to the adverse pressure gradient, and a region of flow reversal can be seen on the upper surface of the flap in Fig. 13.

Figure 14 is a typical view of the projection of velocity vectors onto a vertical, chordwise plane at a mid-semispan location—here corresponding to $2y/b = 0.53$ ($b/2$ is the wing semispan). Note the leading-edge-to-trailing-edge bias to the flowfield due to rotor swirl. The location of the stagnation region is well forward of the midchord region—in the absence of swirl, computations have shown the rotor flowfield is near symmetric about a vertical line through the midchord location. The vortices shed from the leading and the trailing edge are clearly visible in the wake region beneath the wing. Figure 15 is a magnified view of the velocity vectors at the wing leading edge at this spanwise station, clearly showing the flow separation.

Figure 16 is a comparison of computed and measured wing surface pressures at three different spanwise locations: $2y/b = 0.145$, 0.705, and 0.891. The edge of the rotor disk passes over the wing at $2y/b = 0.20$, and so $2y/b = 0.145$ is outside of the rotor wake and in the region of the recirculating fountain. The pressures are relative to freestream ambient and are normalized by rotor thrust loading T/A. Also, x/c is the distance from the leading edge, normalized by the undeflected flap wing chord. Because of the unsteadiness in the wake that causes small amplitude periodic fluctuations in download, the pressures have been time averaged over one period of oscillation of the download/thrust ratio DL/T. The experimental

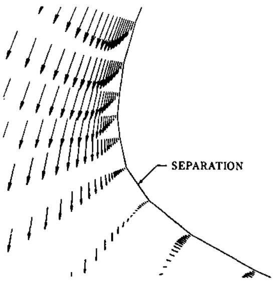

Fig. 15 Magnified view of instantaneous velocity vectors around the leading edge at $2y/b = 0.53$.

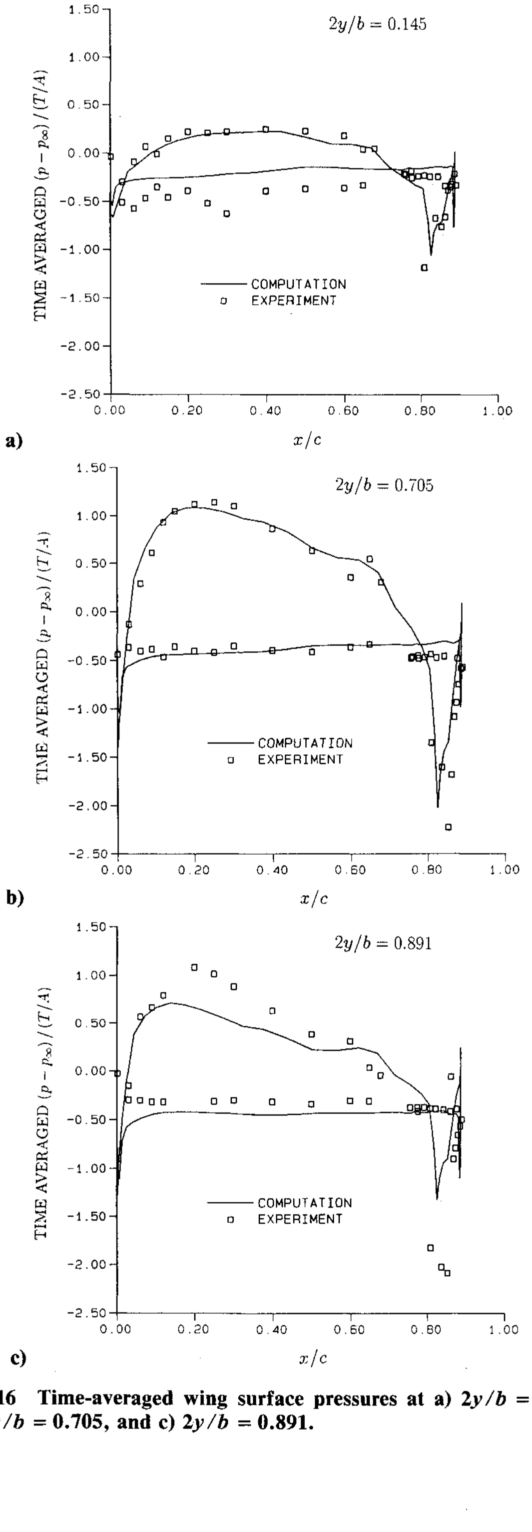

Fig. 16 Time-averaged wing surface pressures at a) $2y/b = 0.145$, b) $2y/b = 0.705$, and c) $2y/b = 0.891$.

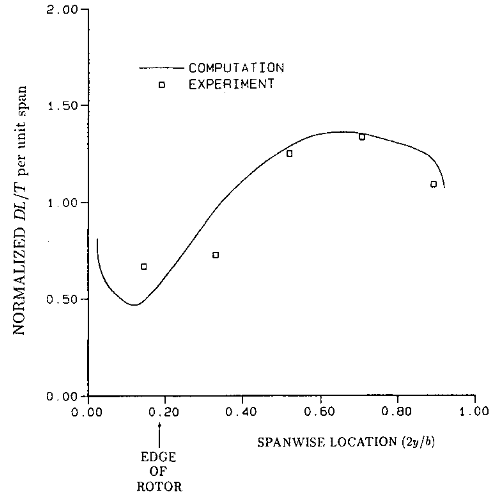

Fig. 17 Comparison between computed and measured values of normalized time-averaged download/thrust per unit span.

results are taken from a 0.658-scale V-22 wing/rotor test at the NASA Ames 40- × 80-ft wind tunnel.[27] The upper surface pressures are fairly well predicted except in the outboard region of the wing where the computation shows significant spanwise flow toward the tip. This accounts for the reduced pressure on the upper surface at $2y/b = 0.891$ compared to experiment. The base pressure at $2y/b = 0.705$ agrees very well with the experimental measurements. At $2y/b = 0.145$, however, the computed base pressure is higher than measured experimentally. This is consistent with the computed weaker fountain flow, which encourages later flow separation on the wing leading edge. At $2y/b = 0.891$, the computed base pressure is lower than the corresponding measured values due to a larger extent of three-dimensional flow predicted for the lower surface near the wingtip.

Figure 17 compares the computed and measured[27] time-averaged download/thrust per unit span normalized by the total time-averaged download/thrust. This figure shows the spanwise variation of the effect of the rotor flowfield on the wing. The computed distribution generally follows the shape of the experimental distribution. As mentioned previously, the edge of the computed rotor wake is diffused, and this contributes to the more gradual download gradient spanwise in the region $0.2 < 2y/b < 0.5$. Greater grid point density, particularly in the region of the edge of the rotor slip stream, is required to compute the spanwise download distribution more accurately. The local increase in download/thrust near the wing centerline, produced by the change in momentum due to the flow turning away from the surface in the recirculation fountain, is predicted by the computation. There is insufficient experimental data to observe this effect.

The computed total download/thrust (DL/T) is higher than measured. At a flap setting of 67 deg, a DL/T of 0.091 was measured in the test reported in Ref. 26. This compares to 0.113 obtained computationally. This discrepancy can be attributed to several factors. The actual rotor plane and wing are not coplanar, as mentioned earlier. This is expected to contribute to the lower measured download, relative to the computed value. Grid refinement studies are required to determine the solution sensitivity to the number and distribution of grid points. The size of the grid used in this study was determined by the eight megaword limit on computer memory per user on the NASA Ames Cray Y-MP computer at the time these computations were performed. The Baldwin-Lomax turbulence model employed in this study is not particularly suited to this computation as it was developed for relatively benign airfoil flows at low angle of incidence. Also, the thin-layer Navier-Stokes equations do not fully represent the complex separated flow in the region beneath the wing.

Conclusions

Computations of wing/rotor interaction about a simplified tilt rotor configuration in hover have been performed. The unsteady, thin-layer Navier-Stokes equations are solved using a time-accurate, implicit, finite difference solution algorithm. The results obtained are very encouraging. The ability of the actuator disk representation of the rotor to predict the mean characteristics of the rotor flowfield has been demonstrated. The major flow features of wing/rotor interaction for the tilt rotor configuration are computed by the numerical method. Differences between computed and experimental results can be partly attributed to differences in geometry between the actual and the numerical models. Further grid refinement is required to better resolve the circumferential edge of the rotor wake. Better comparisons with experiment could also be obtained by modeling more fully the actual geometry including the fuselage, nacelle, and rotor hub. Improved representation of the separated flow region beneath the wing would require solution of the full Navier-Stokes equations and development of a more suitable turbulence model. Despite these limitations, the method, in its current state of development, can provide a useful tool for the study of the relative effects of flap deflection, direction of rotor rotation, circulation control by blowing, etc., on wing download.

Acknowledgments

The authors wish to thank the Rotorcraft Aeromechanics Branch of NASA Ames Research Center for its support under Contract NCC-2-55 and for the computer time on the Cray Y-MP. Also, the authors would like to acknowledge the helpful discussions with Shigeru Obayashi, Domingo Tavella, and Jim McCroskey and his research group, all of NASA Ames, as well as David Yeh of Rockwell International.

References

[1] Felker, F. F., "A Review of Tilt/Rotor Download Research," 14th European Rotorcraft Forum, Paper 14, Milan, Italy, Sept. 1988.

[2] Felker, F. F., and Light, J., "Rotor/Wing Aerodynamic Interactions in Hover," NASA TM 88255, May 1986.

[3] McVeigh, M. A., "The V-22 Tilt-Rotor Large-Scale Rotor Performance/Wing Download Test and Comparison with Theory," 11th European Rotorcraft Forum, Paper 97, London, Sept. 1985.

[4] Srinivasan, G. R., Baeder, J. D., Obayashi, S., and McCroskey, W. J., "Flowfield of a Lifting Hovering Rotor—A Navier-Stokes Simulation," 16th European Rotorcraft Forum, Paper I.3.5, Glasgow, Scotland, UK, Sept. 1990.

[5] Clark, D., and McVeigh, M., "Analysis of the Wake Dynamics of a Typical Tilt-Rotor Configuration in Transition Flight," 11th European Rotorcraft Forum, Paper 28, London, 1985.

[6] Clark, D., "Analysis of the Wing/Rotor and Rotor/Rotor Interactions Present in Tilt-Rotor Aircraft," *Vertica,* Vol. 11, No. 4, 1987, pp. 731–749.

[7] McCroskey, W., Spalart, P., Laub, G., Maisel, M., and Maskew, B., "Airloads on Bluff Bodies, with Application to the Rotor-Induced Downloads on Tilt-Rotor Aircraft," *Vertica,* Vol. 9, No. 1, 1985, pp. 1–11.

[8] Lee, C. S., "A Two Dimensional Study of Rotor/Airfoil Interaction in Hover," Stanford Univ., JIAA TR-88, Stanford, CA, Aug. 1988.

[9] Raghavan, V., McCroskey, W. J., Van Dalsam, W. R., and Baeder, J. D., "Calculations of the Flow Past Bluff Bodies, Including Tilt-Rotor Wing Sections at $\alpha = -90°$," AIAA 28th Aerospace Sciences Meeting, Paper 90-0032, Reno, NV, Jan. 1990.

[10] Pulliam, T., and Steger, J., "Implicit Finite-Difference Simulations of Three-Dimensional Compressible Flow," *AIAA Journal,* Vol. 18, No. 2, 1980.

[11] Fujii, K., and Obayashi, S., "Navier-Stokes Simulation of Transonic Flow over Wing-Fuselage Combinations," AIAA 4th Applied Aerodynamics Conference, Paper 86-1831, San Diego, CA, June 1986.

[12] Fujii, K., and Obayashi, S., "Practical Applications of New LU-ADI Scheme for the Three-Dimensional Navier-Stokes Computation of Transonic Viscous Flows," AIAA 24th Aerospace Sciences Meeting, Paper 86-0513, Reno, NV, Jan. 1986.

[13] Meakin, R., and Suhs, N., "Unsteady Aerodynamic Simulation of Multiple Bodies in Relative Motion," AIAA 9th CFD Conference, Paper 89-1996, Buffalo, NY, June 1989.

[14] Pulliam, T., and Chaussee, D., "A Diagonal Form of an Implicit Approximate-Factorization Algorithm," *Journal of Computational Physics,* Vol. 39, 1981, pp. 347–363.

[15] Steger, J., and Warming, R., "Flux Vector Splitting of the Inviscid Gasdynamic Equations with Application to Finite-Difference Methods," *Journal of Computational Physics,* Vol. 40, 1981, pp. 263–293.

[16] Lombard, C., Bardina, J., Venkatapathy, E., and Oliger, J., "Multi-Dimensional Formulation of CSCM—An Upwind Flux Difference Eigenvector Split Method for the Compressible Navier-Stokes Equations," AIAA 6th CFD Conference, Paper 83-1895, Danvers, MA, July 1983.

[17] Obayashi, S., and Guruswamy, G. P., "Unsteady Shock-Vortex Interaction on a Flexible Delta Wing," 32nd AIAA/ASME/ASCE/AHS/ASC Structures, Structural Dynamics and Materials Conference, Paper 91-1109, Baltimore, MD, April 1991.

[18] Vinokur, M., "Conservation Equations of Gasdynamics in Curvilinear Coordinate Systems," *Journal of Computational Physics,* Vol. 14, 1974, pp. 105–125.

[19] Obayashi, S., "Numerical Simulation of Underexpanded Plumes Using Upwind Algorithms," AIAA Atmospheric Flight Mechanics Conference, Paper 88-4360, Minneapolis, MN, Aug. 1988.

[20] Obayashi, S., Fujii, K., and Gavali, S., "Navier-Stokes Simulation of Wind-Tunnel Flow Using LU-ADI Factorization Algorithm," NASA TM 100042, Feb. 1988.

[21] Sorenson, R., and Steger, J., "Numerical Generation of Two-Dimensional Grids by the Use of Poisson Equations with Grid Control at Boundaries," *Proceedings of the Numerical Grid Generation Techniques Workshop,* NASA CP-2166, NASA Langley Research Center, Hampton, VA, 1980, pp. 449–461.

[22] Glauert, H., *The Elements of Airfoil and Airscrew Theory,* Cambridge University Press, London, 1930.

[23] Prouty, R. W., *Helicopter Performance, Stability, and Control,* PWS Publishers, Boston, MA, 1986.

[24] Rajagopalan, R. G., and Mathur, S. R., "Three Dimensional Analysis of a Rotor in Forward Flight," AIAA 20th Fluid Dynamics, Plasma Dynamics and Lasers Conference, AIAA Paper 89-1815, Buffalo, NY, June 1989.

[25] Yu, N. J., Samant, S. S., and Rubbert, P. E., "Flow Prediction for Propfan Configurations Using Euler Equations," AIAA 17th Fluid Dynamics, Plasma Dynamics and Lasers Conference, Paper 84-1645, Snowmass, CO, June 1984.

[26] Felker, F., Signor, D., Young, L., and Betzina, M., "Performance and Loads Data From a Hover Test of a 0.658-Scale V-22 Rotor and Wing," NASA TM 89419, April 1987.

[27] Felker, F., Shinoda, P., Heffernan, R., and Sheehy, H., "Wing Force and Surface Pressure Data from a Hover Test of a 0.658-Scale V-22 Rotor and Wing," NASA TM 102244, Feb. 1990.